inorganics

MDPI

Article

Bulk Physical Properties of a Magnetic Weyl Semimetal Candidate NdAlGe Grown by a Laser Floating-Zone Method

Naoki Kikugawa [1,*], Taichi Terashima [1], Takashi Kato [2,3], Momoko Hayashi [2], Hitoshi Yamaguchi [2] and Shinya Uji [1]

[1] National Institute for Materials Science, Ibaraki 305-0003, Japan
[2] National Institute for Materials Science, Ibaraki 305-0047, Japan
[3] National Institute of Technology, Fukushima College, Fukushima 970-8034, Japan
* Correspondence: kikugawa.naoki@nims.go.jp

Abstract: In this study, we report the successful growth of single crystals of a magnetic Weyl semimetal candidate NdAlGe with the space group $I4_1md$. The crystals were grown using a floating-zone technique, which used five laser diodes, with a total power of 2 kW, as the heat source. To ensure that the molten zone was stably formed during the growth, we employed a bell-shaped distribution profile of the vertical irradiation intensity. After the nominal powder, crushed from an arc-melted ingot, was shaped under hydrostatic pressure, we sintered the feed and seed rods in an Ar atmosphere under ultra-low oxygen partial pressure ($<10^{-26}$ atm) generated by an oxygen pump made of yttria-stabilized zirconia heated at 873 K. Single crystals of NdAlGe were successfully grown to a length of 50 mm. The grown crystals showed magnetic order in bulk at 13.5 K. The fundamental physical properties were characterized by magnetic susceptibility, magnetization, specific heat, thermal expansion, and electrical resistivity measurements. This study demonstrates that the magnetic order induces anisotropic magnetoelasticity, magneto-entropy, and charge transport in NdAlGe.

Keywords: NdAlGe; magnetic Weyl semimetal; crystal growth; laser floating-zone technique; bulk physical properties

Citation: Kikugawa, N.; Terashima, T.; Kato, T.; Hayashi, M.; Yamaguchi, H.; Uji, S. Bulk Physical Properties of a Magnetic Weyl Semimetal Candidate NdAlGe Grown by a Laser Floating-Zone Method. *Inorganics* **2023**, *11*, 20. https://doi.org/10.3390/inorganics11010020

Academic Editor: W. Adam Phelan

Received: 1 December 2022
Revised: 21 December 2022
Accepted: 25 December 2022
Published: 1 January 2023

1. Introduction

Weyl semimetals have been rapidly advanced as a topologically nontrivial phase of matter. As the low-energy, excited quasiparticles are characterized by relativistic fermions, the electronic structures yield exotic physical phenomena such as Fermi arcs and chiral anomaly [1–5]. The topological Weyl semimetals can be realized when either the spatial inversion or time-reversal symmetry is broken. As well as these semimetals, magnetic topological materials have attracted much attention because the interplay between their magnetic correlations and topological electronic structures can provide rich physical properties. Novel magnetoresistance, anomalous Hall and Nernst effects, axion insulator, and chiral domain walls have been experimentally revealed in several materials [6–9]. Establishing a fundamental framework of magnetic Weyl semimetals is a demand for the next generation of spintronics applications, such as high-density and high-speed memory devices, and quantum information technology, because development of these technologies is based on the intrinsic physical properties of the Weyl semimetals [10].

The *RAlT* family (*R*: lanthanides, *T*: Si, Ge) with the space group $I4_1md$ (No. 109) has been considered to be a candidate material in a new class of magnetic topological semimetals, because the system breaks both the spatial inversion and time-reversal symmetries [11]. The crystal structure of *RAlT* is shown in Figure 1. As theoretically predicted [12], the reports of topological magnetic order [13,14], topological Hall effect [15], anomalous Hall and Nernst effects [16–18], unusual quantum oscillatory effect [14,19,20], possible axial gauge fields [17], domain wall chirality [21], and Fermi arcs [22] have revealed that *RAlT*

can offer rich electromagnetic properties. Since these properties can be tuned by exchanging the rare-earth elements (*R*) and *T* [17], this motivates us to systematically explore the relationship between the topology and magnetism in the *R*Al*T* family.

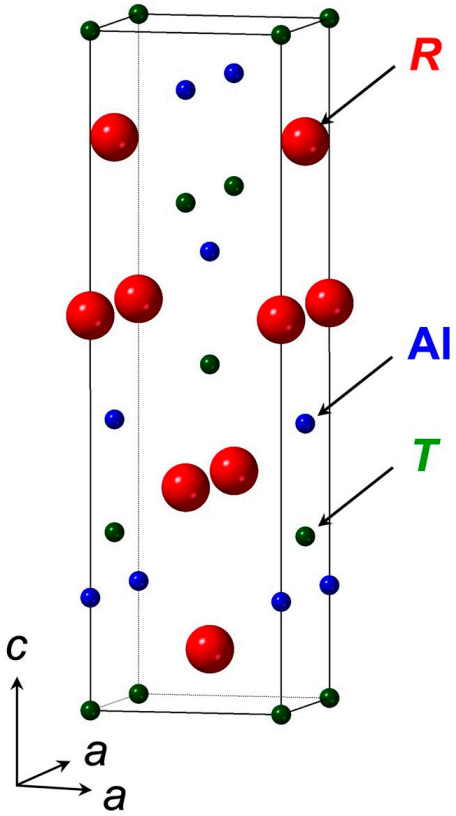

Figure 1. Crystal structure of a magnetic Weyl semimetal candidate *R*Al*T* (*R*: rare earth element, *T*: Si, Ge), with the space group $I4_1md$ (No. 109).

Thus far, a series of flux-grown crystals of *R*Al(Si,Ge) with *R* = Ce, Pr, Nd, and Sm, has been investigated [11,14,16–19,21–23], whereas floating-zone crystals have been examined only in CeAlGe and PrAlGe [11,15,17]. The floating-zone method offers two main advantages: (1) it minimizes the contamination level during the growth process, (2) it can obtain large crystals in cm size [24–26]. This enables us to deepen our knowledge of the materials through several experimental probes of the same batch of crystals. In this paper, we present the successful growth of NdAlGe crystals with the length of 50 mm by the floating-zone method, adopting laser diodes as the heat source. We demonstrate the fundamental physical properties of NdAlGe, focusing on its anisotropic response with magnetic order at 13.5 K.

2. Materials and Methods

2.1. Crystal Growth by the Floating-Zone Method

Crystal growth by using the floating-zone method is mainly composed of a polycrystalline feed-rod, molten zone, and a seed/grown crystal. As these components never touch any other part of the apparatus (including the quartz tube) throughout the growth, the growing crystal is protected from accidental contamination of any kind of impurity [24–26]. However, as the molten zone is fragilely supported only at the edges of the feed and seed rods, it is easily destabilized. Maintaining a stable molten zone requires great care and the optimizing of many parameters, such as the heat power required to melt the rods, the feed/seed speed, the gas atmosphere, and the applied pressure. In this study, the NdAlGe growth was kept stable by employing a laser diode as the heat source, and preparing a

feed/seed rod: the latter has been successfully applied to oxides in previous studies [27]. These two stabilization techniques are described in detail below.

2.2. Laser Floating-Zone Technique

The recently developed laser-based floating-zone technique has opened a new window for crystal growth, because the laser diode enables the growth of materials that have not been obtained under optical halogen/xenon lamps connected to an infrared image furnace, which is used as the conventional heat source [28]. The laser emission can sharply define the focal point of melting, forming a narrower molten zone than can be achieved by radiation from lamps reflected at the elliptical mirrors of an image furnace [29]. Consequently, the laser-heated molten zone is homogeneous and tolerates a steeper temperature gradient at the boundary between the molten zone and the grown crystal. Most recently, the distribution profile of the vertical irradiation intensity along the length of the rod has progressed from flat to bell-shaped, where the original flat horizontal profile was maintained along the radical direction of the rod (see Figure 2 of [30]). The new bell-shaped distribution is a significant advance because it relaxes the thermal stress in the grown crystals. The modified temperature gradient imposed by the bell-shaped distribution prevents the as-grown crystals from cracking. Crystals grown under the original flat laser profile are frequently cracked by the too-sharp temperature gradient developed at the boundary [30]. Thus, modern laser technology has dramatically advanced the crystal growth field in recent years [29–31]. We grew single-crystalline NdAlGe using a laser diode floating-zone furnace, in which five laser diodes produce a vertical bell-shaped distribution around the focal point.

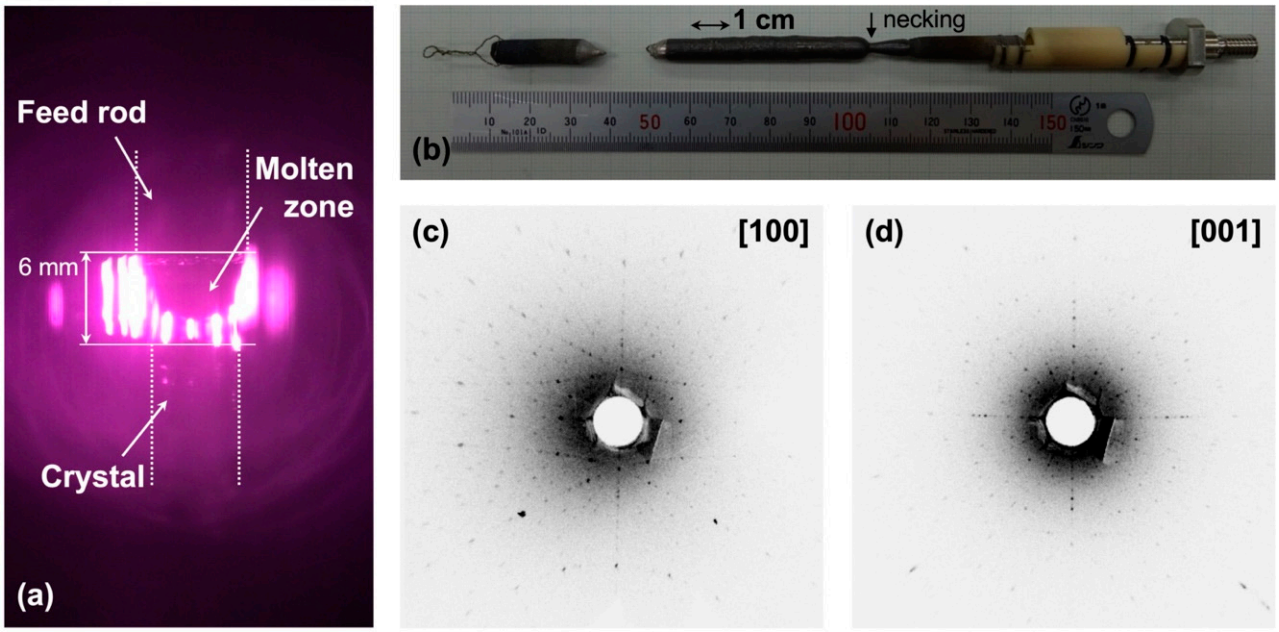

Figure 2. (**a**) Picture of crystal growth of NdAlGe using a laser diode heated floating-zone furnace. Dotted white lines outline the rod and grown crystal for clarity. (**b**) Photograph of the grown NdAlGe crystal showing the necking formed at the beginning of the growth; (**c**) and (**d**) back-scattered Laue photographs along the [100] and [001] axes, respectively.

2.3. Preparation of Feed and Seed Rods

The floating-zone technique has grown intermetallic compounds, as well as oxides and chalcogenides [28–35]. Feed rod preparation is an important procedure for the entire growth process because the quality of the feed rods strongly affects the stability of the molten zone. In particular, the feed rods must be well-shaped, and mechanically robust with uniform density and composition [36]. The rods for intermetallic alloys have been conventionally shaped by melting the starting materials in an arc furnace or a radio-

frequency induction-heating furnace. However, these methods may introduce cracks inside the resultant rods, and the cracks prevent a stable form of the molten zone during the crystal growth. An alternative advanced method has been reported, consisting of designing a modified radio-frequency induction-heating furnace [36].

We prepared a polycrystalline feed rod of NdAlGe by the following process. First, we prepared polycrystalline ingots of NdAlGe with a nominal composition via arc-melting under an Ar atmosphere (Techno Search Corp., SE-11399). The button-shaped ingot was turned over and melted several times to ensure homogeneity. The arc-melted ingots were subsequently powdered using an agate mortar and pestle. The powder with a typical weight of 18 g was packed into a tubular rubber balloon for shaping into a cylindrical rod. The powder-filled balloon was pressed under hydrostatic pressure at 40 MPa for 5 min. Here, to avoid the contamination from the as-purchased balloon of which surfaces were coated with a fine powder, we carefully cleaned both the inner and outer surfaces of the balloon before filling the NdAlGe powder, as experienced from the growth of ruthenates [27]. After their removal from the balloon, the uniform-shaped rods were sintered at 1123 K for 24 h in a tube furnace under an Ar gas flowing at 3 L/min. The Ar gas was regenerated using an oxygen pump made of yttria-stabilized zirconia heated at 873 K and circulated under an ultra-low oxygen partial pressure of less than 10^{-26} atm (Canon Machinery Inc., ULOCE-530) [37]. Finally, the sintered rod with a typical diameter of 6 mm was cut into two unequal parts. The longer part, with a length of 80 mm, was designated as the feed rod and the shorter part, with a length of 30 mm, was used as the seed. High-quality ruthenates were previously grown by a similar procedure [27,38–43]. This process obtained homogeneous rods with a minimal contamination risk; consequently, a series of ruthenate crystals was successfully grown under stable conditions, with no accidental cracks to the rods during irradiation in the furnace [27,39,41–43]. We note that the procedure can be applied to that for the growth of intermetallic alloys.

2.4. Crystal Growth

Both the feed and seed rods were set into a laser diode floating-zone furnace equipped with five 400 W GaAs-based laser heads with a wavelength of 940 nm (L-FZ 2000, Quantum Design Japan). Here, the bell-shaped distribution profile of the vertical irradiation intensity was optimized. The feed rod was suspended from a hock (made of platinum) on the upper shaft using molybdenum wire, and the seed rod was set in an alumina holder on the lower shaft. Since the growth area of the furnace was separated by a quartz tube from the outside, we could select the desired atmosphere and pressure of the gas during the crystal growth. For the growth of NdAlGe, we used a gas mixture of Ar (96%) and H_2 (4%). As the laser power was smoothly increased, the bottom end of the rod started to melt. The molten rod was then connected to the top of the seed rod. The growth started with necking because a polycrystalline rod was used as the seed. Once the necking was complete, the molten zone was stabilized at both feed and seed speeds of 5 mm/h in the Ar-H_2 gas mixture at 0.4 MPa and with a flow rate of 1 L/min. Applying the pressure to 0.4 MPa was in order to attempt the suppression of the evaporation during the growth. The feed and seed were rotated at 10 rpm in opposite directions to homogenize the molten liquid. The molten zone remained stable until the end of the growth without any cracking or other accidental issues arising from the sintered rods prepared by the above procedure.

2.5. Characterization

The phase purity of the crushed single crystals was checked using power X-ray diffraction under Cu *Kα* radiation (MiniFlex600, Rigaku) at room temperature. To cut the grown crystals along their principle crystallographic axes (the *a* and *c* axes), the orientations of the crystals were checked by a back-scattered X-ray Laue diffraction technique. The composition of the grown crystal was determined using inductively coupled plasma optical emission spectrometry (ICP-OES).

The bulk physical properties were measured down to 2 K using the options of the Physical Property Measurement System (Dynacool, Quantum Design). The temperature dependence of the magnetic susceptibility was measured in a magnetic field (H) of 0.01 T under zero-field-cooled (ZFC) and field-cooled (FC) conditions: that is, by cooling the sample before and after applying a static magnetic field, respectively. The isothermal magnetization (M) was measured between −9 and 9 T. The temperature dependence of the specific heat (C_P) was measured by a relaxation method. The thermal expansion was measured by a capacitive-based technique with a temperature sweep of 0.1 K/min. In the thermal expansion measurements, we used a fused quartz dilatometer cell because fused quartz has the weakest temperature dependence among the known thermally expansive materials [44]. The magnetic entropy change (ΔS_M) of $H//a$ and $H//c$ was determined using the thermodynamic Maxwell relation, $\Delta S_M = \int_0^H \frac{\partial M}{\partial T} dH$ [45], obtained from the temperature dependence of the magnetization up to 9 T under the FC process. The magnetic susceptibility, magnetization, specific heat, and thermal expansion measurements were measured on the same sample with dimensions of 2.0 mm after cutting and polishing along the a and c axes. The electrical resistivity was measured by the standard four-probe AC method, after spot-welding electrical contacts on the rectangular-shaped crystals. We also examined measurements of the a-axis resistivity of the crystals in a top-loaded dilution fridge.

3. Results and Discussion

3.1. Crystal Growth

Figure 2a shows a photo of the crystal growth of NdAlGe. The bell-shaped distribution, created by the five laser diodes, focused on the molten zone with a length of 6 mm. The rod was not cracked by the laser emission during the growth. As seen in Figure 2b, crystals with a length of 50 mm were grown under stable conditions. Additionally, there were no signs on the surface of the grown crystals that the molten liquid was dropped during the growth, suggesting that the growth was performed under stable temperature control. Figure 3 displays the powder diffraction pattern of a partially crushed crystal. All peaks were well indexed to the space group $I4_1md$ [11] and no impurity phases were detected. The lattice parameters were deduced as a = 0.42245(13) nm, and c = 1.4576(6) nm, consistent with previous reports on polycrystals [46] and flux-grown crystals [23]. Figure 2c,d show the back-scattered Laue photographs of the grown crystal along the [100] and [001] directions, respectively. Clear and sharp spots from the bulk crystal confirmed that a large single crystal was obtained. From the ICP-OES results, the molar ratio of the grown crystal was determined as Nd: Al: Ge = 1.00: 0.93: 0.98. The ratio was identical along the crystal rods within the experimental error, suggesting the grown crystal is homogeneous. The aluminum deficiency reflects the evaporation of aluminum during the growth. The evaporated powder was deposited on the inside surface of the quartz tube.

3.2. Bulk Properties of the Grown Crystal

The temperature dependences of the magnetic susceptibility (M/H) were measured in a field of 0.01 T. The results along the a and c axes are presented in Figure 4a,b, respectively. A clear magnetic transition (T_M) appears at 13.5 K in both field directions. The transition temperature of our floating-zone crystal exceeded that of the flux-grown crystals [23]. Here, T_M defines the temperature at which clear hysteresis occurs between the ZFC and FC processes. Such hysteresis can be attributed to pinning of the magnetic domains below the magnetic ordering temperature. We also observe a large anisotropy of the magnetic susceptibility below T_M between $H//a$ and $H//c$, as seen in the flux-grown crystal [23]. Figure 4c,d plot the temperature dependence of the inverse magnetic susceptibility $(M/H)^{-1}$ along the a and c axes, respectively. The black lines in the figures are the fits to the Curie–Weiss law, $\frac{M}{H} = \frac{N_A \mu_{eff}^2 \mu_B^2}{3k_B(T-\theta_P)} + \chi_0$, where k_B, N_A, μ_B are the Boltzmann constant, Avogadro's number, and the Bohr magneton, respectively. From the fits between 100 and 300 K, the effective magnetic moments (μ_{eff}) in the paramagnetic region were μ_{eff} = 3.57 μ_B

and 3.66 μ_B under *H*//*a* and *H*//*c*, respectively. These values are very close to the theoretical value of the free Nd^{3+} with a total angular momentum of $J = 9/2$, which corresponds to $\mu_{eff} = 3.62\ \mu_B$. The results suggest a well-localized nature of the 4*f* electrons. The small temperature-independent term χ_0, which typically represents Pauli paramagnetic and Larmor diamagnetic contributions, was 8.14×10^{-4} (4.82×10^{-4}) emu/mol for *H*//*a* (*H*//*c*). The Weiss temperatures under *H*//*a* and *H*//*c* were obtained as $\theta_P = -4.4$ K and +11.4 K, respectively. Here, the negative and positive θ_P indicate an antiferromagnetic correlation and ferromagnetic coupling, respectively.

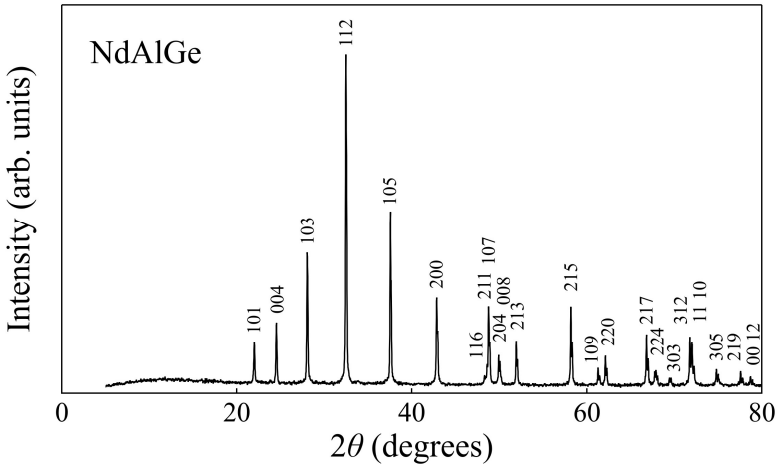

Figure 3. Powder X-ray diffraction pattern showing the indices of crushed NdAlGe crystal (Cu *Kα* radiation at room temperature).

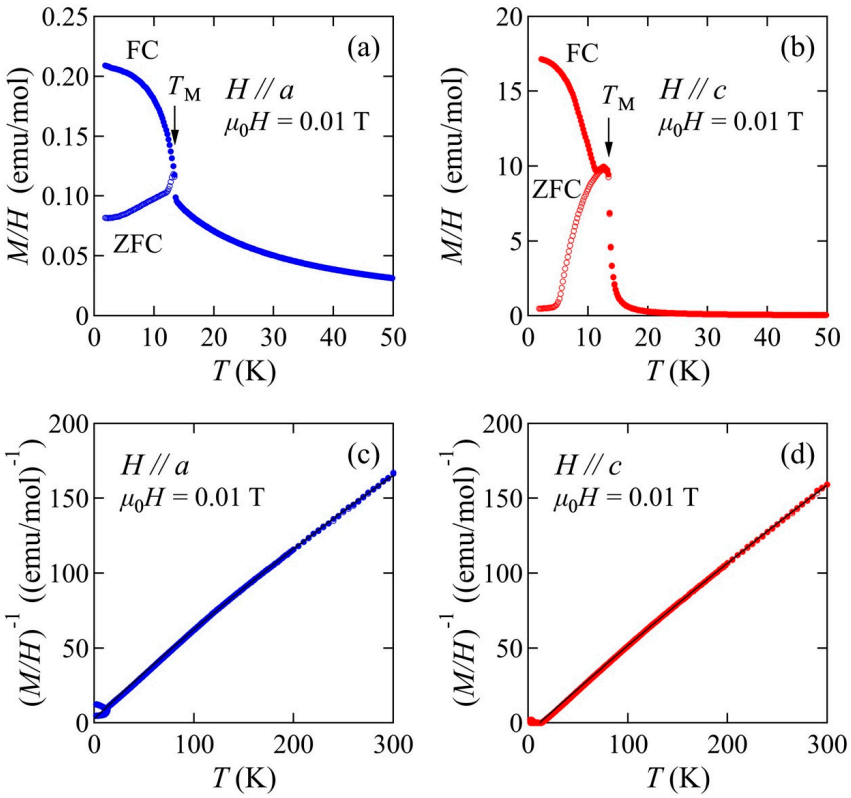

Figure 4. Temperature dependences of the magnetic susceptibility of NdAlGe under the field along (**a**) *H*//*a* and (**b**) *H*//*c*. Measurements were performed under zero-field-cooled (open circles) and field-cooled (closed circles) processes at 0.01 T. Inverse magnetic susceptibility as a function of temperature under (**c**) *H*//*a*, and (**d**) *H*//*c*. Solid black lines are fits to the Curie–Weiss law between 100 and 300 K.

The anisotropy of the magnetic property was observed by the isothermal magnetization at 2 K under *H*//*a* and *H*//*c* up to 9 T (Figure 5a). Figure 5b enlarges the low-field region to emphasize the obvious hysteresis under *H*//*c*. The overall behavior is similar to that observed in flux-grown crystals, in which measurements were performed up to 30 T [23]. The magnetization under *H*//*c* shows a clear hysteresis with a remnant magnetization and a small coercive field of 0.07 T, indicating magnetic order with a spontaneous magnetization. In contrast, the *a*-axis magnetization shows no clear hysteresis and is nearly 100 times smaller than the *c*-axis magnetization at 0.3 T. The *a*-axis magnetization is linear in *H* up to 2 T and slightly deviates upwards at higher field. The strong anisotropy suggests that NdAlGe has an Ising-like magnetism with the *c* axis being the easy axis.

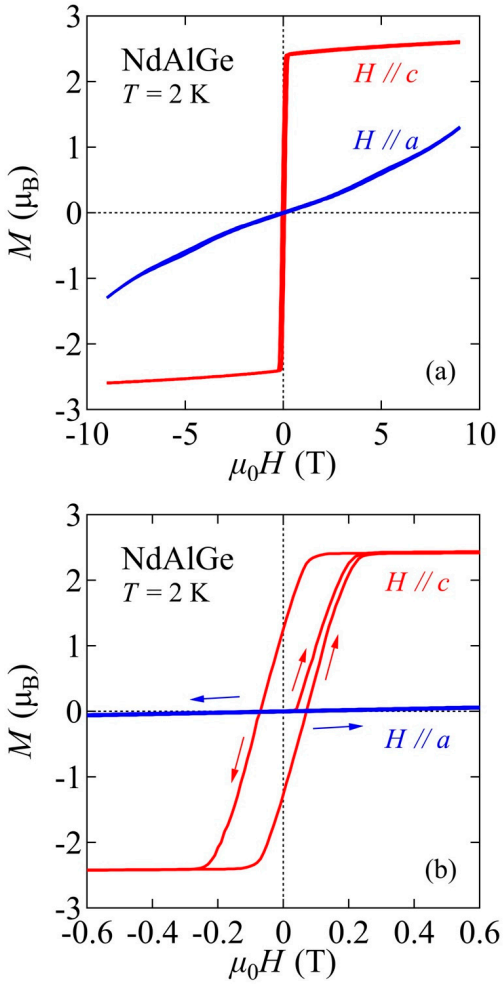

Figure 5. (**a**) Isothermal magnetization of NdAlGe at 2 K under *H*//*a*, and *H*//*c* between –9 and +9 T. (**b**) Zoom-in of the low-field region between –0.6 and +0.6 T to emphasize the hysteresis under *H*//*c*.

Figure 6a,b plot the isothermal magnetization of NdAlGe under *H*//*a*, and *H*//*c*, respectively, at several temperatures across the T_M. These data were taken after field cooling. Under *H*//*c*, the rapid increase in magnetization at low fields was suppressed as the temperature increased. The remnant magnetization disappeared at T_M. Under *H*//*a*, the upward behavior observed at 2 K was suppressed as the temperature was raised.

Figure 7a shows the temperature dependence of the specific heat (C_P) without field. We can see a well-defined lambda-type anomaly, as seen in the sister materials *RAl*(Ge,Si) [14,18]. A second-ordered-like transition temperature at 13.5 K, defined as the midpoint of the jump, corresponds accurately to the onset of the magnetic transition at T_M observed in the magnetic susceptibility measurements. Judging from the result, the observed phase transition in NdAlGe occurs in bulk. We mention that only a single peak with a sharp

transition width of less than 0.4 K is seen; no other transitions were detectable at our experimental resolution down to 2 K. Figure 7b plots the temperature dependence of the specific heat divided by temperature (C_P/T). The $\Delta C_P/T$ jumped by 0.69 J/mol K^2 at T_M.

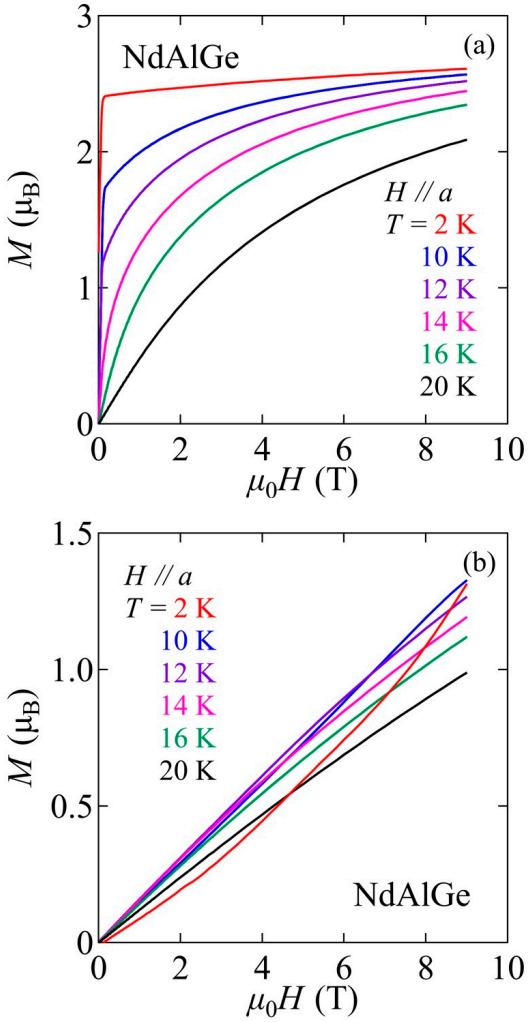

Figure 6. Isothermal magnetization curves of NdAlGe under (**a**) *H*//*a*, and (**b**) *H*//*c* at temperatures below and above the transition temperature at 13.5 K. The data were taken under the field-cooled process.

Thermodynamic phase transitions can be detected through thermal expansion experiments, which provide the directional information along the independent crystallographic axes [47]. In contrast, specific heat measurements probe the overall information on phase transitions, as shown in Figure 7. Figure 8a shows the linear thermal expansions $\frac{\Delta L_i}{L_i} = \frac{L_i(T) - L_i(300\ K)}{L_i(300\ K)}$, where the index i refers to the a and c axes, as functions of temperature. The inset shows the temperature-dependent $\frac{\Delta L_i}{L_i}$ up to 300 K. Both $\frac{\Delta L_a}{L_a}$ and $\frac{\Delta L_c}{L_c}$ show a clear kink (not a discontinuous jump) at T_M = 13.5 K, suggesting a second-ordered phase transition. Moreover, the results are highly anisotropic: on cooling, the thermal expansions along the *a* and *c* axes increase and decrease below T_M, respectively. This result is possibly attributable to the anisotropic magnetic correlations of this material, as discussed for NdAlSi [14]. Figure 8b presents the temperature dependence of the linear thermal expansion coefficient $\alpha_i = \frac{1}{L_i(300\ K)} \frac{d\Delta L_i(T)}{dT}$ along the *a* and *c* axes. Also shown is the volume expansion coefficient α_v deduced as $2\alpha_a + \alpha_c$, considering the tetragonal crystal symmetry of this material. Anomalies in both α_a and α_c correspond to the magnetic transition temperature at T_M, suggesting a strong magnetoelastic coupling in NdAlGe.

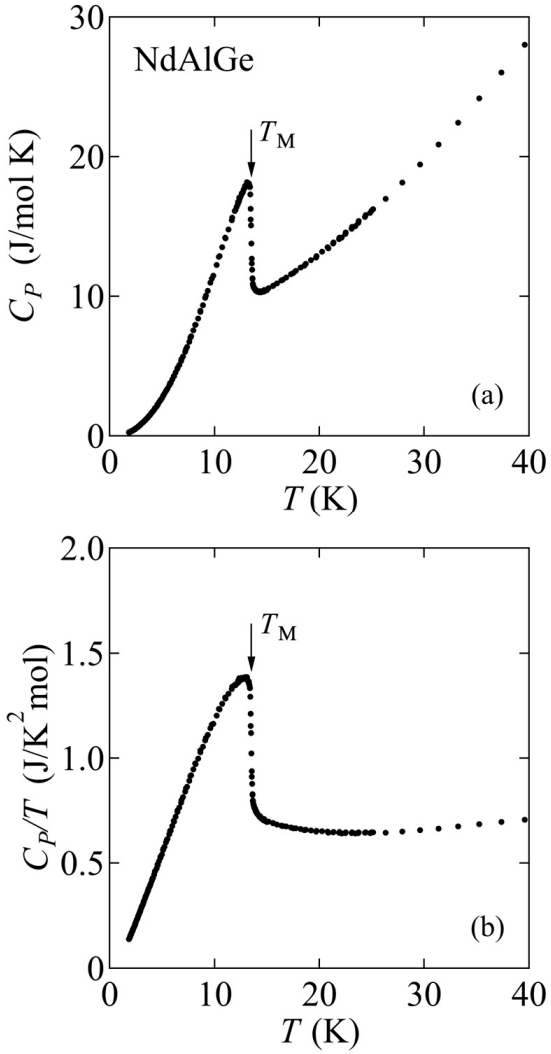

Figure 7. (**a**) Temperature dependence of specific heat (C_P) of NdAlGe under zero field. (**b**) Specific heat divided by temperature (C_P/T) plotted against temperature.

For a second-ordered phase transition, the uniaxial and hydrostatic pressure dependence of the magnetic transition temperature can be determined by the Ehrenfest relation [47] $\frac{dT_M}{dP_i} = \frac{V_m \Delta a_i}{\Delta(C_P/T)}$, where V_m = 3.92 × 10^{-5} m^3/mol is the molar volume, $\Delta(C_P/T)$ defines the jump in the specific heat divided by the temperature (C_P/T) (Figure 7b), and $\Delta\alpha_i$ is the jump in the thermal expansion coefficient at T_M (Figure 8b). Using our experimental results with $\Delta(C_P/T)$ = 0.69 J/mol K^2, $\Delta\alpha_a = -2.2 \times 10^{-6}$ K^{-1}, and $\Delta\alpha_c = +1.2 \times 10^{-5}$ K^{-1}, we obtained $\frac{dT_M}{dP_a}$ = −0.13 K/GPa, and $\frac{dT_M}{dP_c}$ = +0.68 K/GPa under the uniaxial pressure along the *a* and *c* axes, respectively. This result suggests that uniaxial pressure along the *c* axis stabilizes the magnetic ordered state, whereas that along the *a* axis suppresses this state. In addition, the hydrostatic pressure dependence of the magnetic transition temperature $\frac{dT_M}{dP} = 2\frac{dT_M}{dP_a} + \frac{dT_M}{dP_c}$ was obtained as +0.42 K/GPa. The obtained hydrostatic pressure dependence on T_M in NdAlGe is close to that in the sister compounds CeAlGe, and CeAlSi with $\frac{dT_M}{dP}$ = +0.64 K/GPa, and +0.62 K/GPa, respectively, and the signs of all dependencies are positive although the magnetically easy axis in these Ce-based materials reportedly aligns perpendicular to the *c* axis. [20,21]. The same trend of $\frac{dT_M}{dP} > 0$ was seen in a substitution study of $PrAl(Ge_{1-x}Si_x)$; specifically, the magnetic ordered tempera ture monotonically increased with shrinkage as Si was substituted for Ge [18].

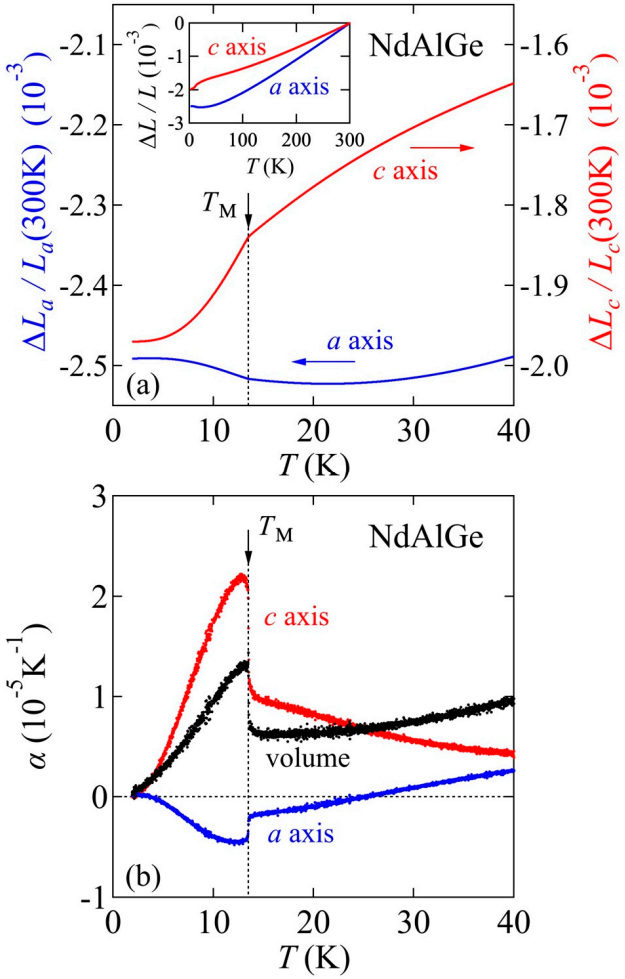

Figure 8. (**a**) Temperature dependences of (**a**) thermal expansion $\frac{\Delta L_i}{L_i} = \frac{L_i(T) - L_i(300\text{ K})}{L_i(300\text{ K})}$ and (**b**) linear thermal expansion coefficient $\alpha_i = \frac{1}{L_i(300\text{ K})} \frac{d\Delta L_i(T)}{dT}$ along the *a* and *c* axes. Indexed by *i*. The volume expansion coefficient α_v, obtained as $2\alpha_a + \alpha_c$ considering the tetragonal crystal symmetry of NdAlGe, is also shown.

The magnetocaloric effect, which determines the correlation between the ordered magnetism and entropy, is worth exploring in magnetic materials. The magnetocaloric effect is a consequence of temperature change (heating or cooling) in a magnetic material under adiabatic conditions when an external magnetic field is applied and removed [48]. The efficiency of the magnetocaloric effect can be evaluated through the magnetic entropy change ΔS_M, defined as the entropy difference between the magnetized material ($S(H)$) and demagnetized material ($S(0)$. Formally, $\Delta S_M = S(H)$–$S(0)$ [45]. The magnetocaloric effect is usually examined in ferromagnetic materials because such materials should, in principle, gain larger ΔS_M through the demagnetized and magnetized process than non-ferromagnetic materials [49–51]. Although evaluating the ΔS_M of NdAlGe with Ising-like magnetization under *H*//*c* (Figure 5a) is an interesting proposition, the ΔS_M of Nd-containing materials are rarely considered because the magnetic moments of materials containing light rare-earth elements are smaller than those of other magnetocaloric materials containing heavy rare-earth elements such as Ho, Gd or transition metal Fe [49–51].

To evaluate the ΔS_M of NdAlGe, we first show the temperature dependences of the magnetization (M vs. T) of NdAlGe under *H*//*a* and *H*//*c* (Figure 9a,b, respectively), under various magnetic fields up to 9 T. These measurements were performed under the FC process. Figure 9c,d present the magnetic entropy changes (ΔS_M) as functions of temperature under *H*//*a*, and *H*//*c*, respectively, for various fields up to 9 T. Here, the ΔS_M

was evaluated from the above-mentioned Maxwell relation. Under *H*//*c*, the ΔS_M shows a single minimum around T_M. The negative magnetic entropy change indicates that the entropy was released/gained under magnetization/demagnetization in NdAlGe. When the field was changed from zero to 5 and 9 T, the ΔS_M values were −4.2 and −5.7 J/K mol, respectively. The value at 5 T was comparable to that in a series of ternary systems summarized in a review article [52], which focused mainly on materials containing heavy rare-earth elements. In contrast, the ΔS_M under *H*//*a* peaked at low temperatures and became negative at higher temperatures. Similar sign-changing behavior is seen in Ni-Mn-Sn alloys [53]. When the field changed to 9 T, the minimum value of ΔS_M under *H*//*a* was −1.3 J/K mol. The positive and negative behavior of ΔS_M under *H*//*a*, and the smaller values than under *H*//*c* might reflect the anisotropic magnetic coupling.

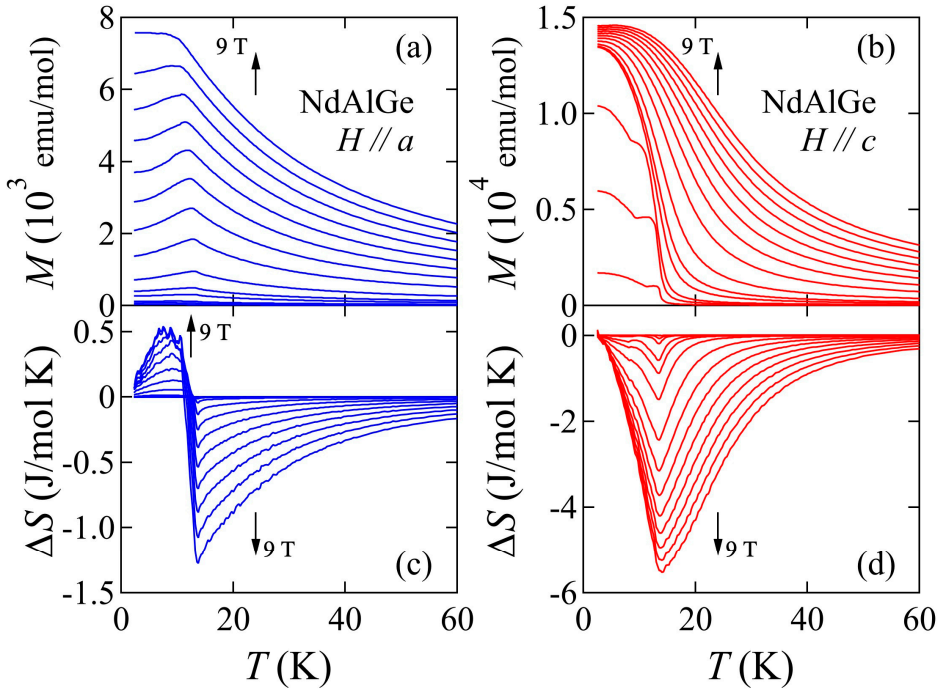

Figure 9. Temperature dependence of magnetization of NdAlGe for (**a**) *H*//*a* and (**b**) *H*//*c* under the field-cooled process. The applied magnetic fields are 0.01, 0.05, 0.1, 0.3, 0.5, 1, 2, 3, 4, 5, 6, 7, 8, and 9 T. The magnetic entropy change ΔS_M as a function of temperature for (**c**) *H*//*a*, and (**d**) *H*//*c*.

The floating-zone technique obtained the large-sized NdAlGe crystals in which we could investigate the directional electrical charge transport properties. Figure 10a presents the temperature dependences of the electrical resistivities ρ_a and ρ_c as the current flow along the *a* and *c* axes, respectively. Figure 10b enlarges the low temperature region. Both ρ_a and ρ_c exhibit metallic behaviors with sublinear temperature dependence at a high temperature. We also mention that the resistive behavior in ρ_a was identical along the radial direction in the grown crystal, suggesting there were homogeneous crystals in the ingot. The residual resistivity ratios (RRRs) were approximately 1.5 and 1.4, respectively. Comparable RRRs were reported in floating-zone crystals CeAlGe and PrAlGe, in which the materials were almost stoichiometric [11,17]. We also mention that the RRRs in our crystals were lower than those seen in the flux-grown crystals [14,16,18,21]. The resistive anisotropy of NdAlGe (ρ_c/ρ_a~2) was almost temperature-independent in the paramagnetic region (above T_M), but the behaviors of ρ_a and ρ_c contrasted below T_M; specifically, ρ_a and ρ_c were suppressed and enhanced below T_M, respectively. In typical magnetic materials, in general, spin scattering and/or reconstruction of the Brillouin zone can influence the scattering rate of the conducting carriers when the system enters the ordered state [54,55]. Suppression of the scattering rate by spin scattering is frequently seen in the magnetic materials, for example, in the ferromagnetic oxide $SrRuO_3$ [42]. Meanwhile, Brillouin zone reconstruction may

enhance the resistivity, as observed in a pressure-induced antiferromagnetic ordered state in FeSe [56]. In NdAlGe, the upturn seen in ρ_c is possibly attributable to a reconstructed zone, whereas the downturn in ρ_a below T_M might be dominated by suppression of the spin scattering.

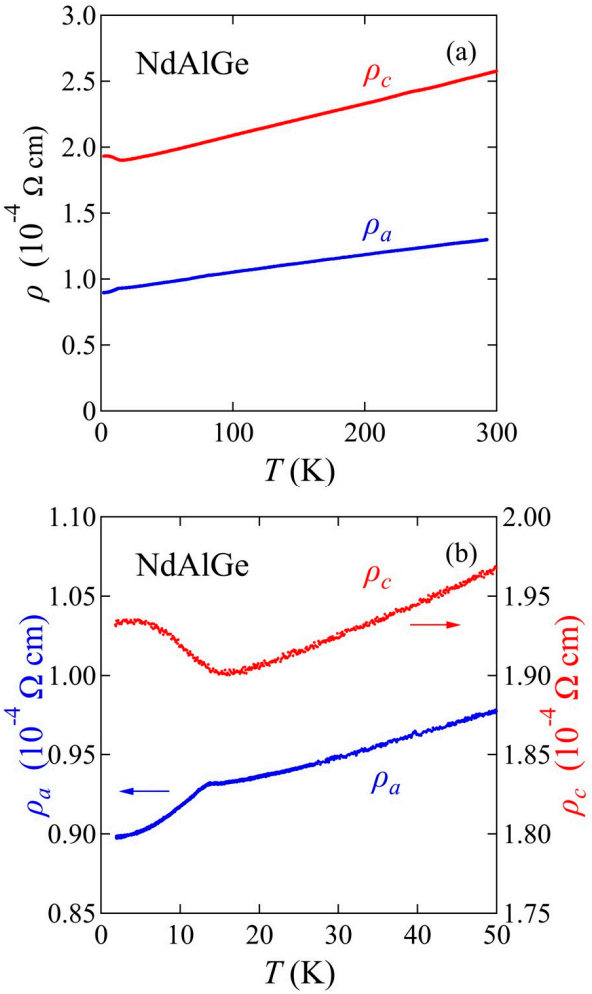

Figure 10. (**a**) Temperature dependence of electrical resistivities ρ_a, and ρ_c under the current flow along the *a* axis and *c* axes, respectively. (**b**) Low temperature resistivities for capturing the anisotropic behavior below the transition temperature.

4. Summary

In summary, we successfully grew single crystals of a magnetic Weyl semimetal candidate NdAlGe using the laser diode heated floating-zone technique. Five laser diodes produced a bell-shaped distribution profile of vertical irradiation intensity. After the nominal powder, crushed from an arc-melted ingot, was shaped under hydrostatic pressure, we sintered the feed and seed rods under Ar gas at ultra-low oxygen partial pressure (<10^{-26} atm). The crystals were grown under the stable conditions of the molten zone without any cracks on the rods. We finally obtained a large-sized crystal with a length of 50 mm. When examined with bulk-sensitive probes, the grown crystals showed magnetic order at 13.5 K. The ordered state presented Ising-like behavior. The magnetic entropy largely changed when a magnetic field was applied along the easy axis (the *c* axis). The linear thermal expansion also confirmed anisotropic responses at the magnetic transition temperature. Applying the thermodynamic Ehrenfest relation based on our experimental data, we revealed the anisotropic uniaxial pressure dependence of the magnetic transition temperature. The hydrostatic pressure dependence on the magnetic transition temperature in NdAlGe was

positively signed, as observed in sister materials of NdAlGe. Anisotropic charge transport below the ordered temperature probably originates from the scattering mechanism.

Author Contributions: N.K. and T.T. conceived the project. N.K. grew and characterized the crystals. T.K., M.H. and H.Y. performed the ICP-OES. S.U. joined the discussion and contributed to the manuscript preparation. wrote the manuscript with input from all coauthors. All authors have read and agreed to the published version of the manuscript.

Funding: This work is supported by a KAKENHI Grants-in-Aids for Scientific Research (Grant Nos. 17H06136, 18K0475, 21H01033, and 22K19093), and a Core-to-Core Program (No. JPJSCCA20170002) from the Japan Society for the Promotion of Science (JSPS), and a JST-Mirai Program (Grant No. JPMJMI18A3).

Data Availability Statement: The data supporting the findings of this study are available from the corresponding authors upon reasonable request.

Acknowledgments: We acknowledge Yoshio Kaneko for fruitful advice about the laser floating-zone furnace, and Takeshi Shimada, Noritaka Kimura, John McArthur, Naohiro Kaga, Yuta Maegawa, Tohru Nagasawa, and Nobuyuki Ochiai for technical support.

Conflicts of Interest: The authors declare no conflict of interest.

References

1. Wang, Z.; Zhang, S.-C. Chiral Anomaly, Charge Density Waves, and Axion Strings from Weyl Semimetals. *Phys. Rev. B* **2013**, *87*, 161107. [CrossRef]
2. Burkov, A.A. Topological Semimetals. *Nat. Mater.* **2016**, *15* 1145. [CrossRef] [PubMed]
3. Yan, B.; Felser, C. Topological Materials: Weyl Semimetals. *Annu. Rev. Condens. Matter Phys.* **2017**, *8*, 337. [CrossRef]
4. Armitage, N.P.; Mele, E.J.; Vishwanath, A. Weyl and Dirac Semimetals in Three-Dimensional Solids. *Rev. Mod. Phys.* **2018**, *90*, 015001. [CrossRef]
5. Nagaosa, N.; Morimoto, T.; Tokura, Y. Transport, Magnetic and Optical Properties of Weyl Materials. *Nat. Rev. Mater.* **2020**, *5*, 621. [CrossRef]
6. Otrokov, M.M.; Klimovskikh, I.I.; Bentmann, H.; Estyunin, D.; Zeugner, A.; Aliev, Z.S.; Gaß, S.; Wolter, A.U.B.; Koroleva, A.V.; Shikin, A.M.; et al. Prediction and Observation of an Antiferromagnetic Topological Insulator. *Nature* **2019**, *576*, 416. [CrossRef]
7. Rienks, E.D.L.; Wimmer, S.; Sánchez-Barriga, J.; Caha, O.; Mandal, P.S.; Růžička, J.; Ney, A.; Steiner, H.; Volobuev, V.V.; Groiss, H.; et al. Large Magnetic Gap at the Dirac Point in $Bi_2Te_3/MnBi_2Te_4$ Heterostructures. *Nature* **2019**, *576*, 423. [CrossRef]
8. Bernevig, B.A.; Felser, C.; Beidenkopf, H. Progress and Prospects in Magnetic Topological Materials. *Nature* **2022**, *603*, 41. [CrossRef]
9. He, Q.L.; Hughes, T.L.; Armitage, N.P.; Tokura, Y.; Wang, K.L. Topological Spintronics and Magnetoelectronics. *Nat. Mater.* **2022**, *21*, 15. [CrossRef]
10. Giustino, F.; Lee, J.H.; Trier, F.; Bibes, M.; Winter, S.M.; Valentí, R.; Son, Y.-W.; Taillefer, L.; Heil, C.; Figueroa, A.I.; et al. The 2021 Quantum Materials Roadmap. *J. Phys. Mater.* **2020**, *3*, 042006. [CrossRef]
11. Puphal, P.; Mielke, C.; Kumar, N.; Soh, Y.; Shang, T.; Medarde, M.; White, J.S.; Pomjakushina, E. Bulk Single-Crystal Growth of the Theoretically Predicted Magnetic Weyl Semimetals *R*AlGe (*R* = Pr, Ce). *Phys. Rev. Mater.* **2019**, *3*, 024204. [CrossRef]
12. Chang, G.; Singh, B.; Xu, S.-Y.; Bian, G.; Huang, S.-M.; Hsu, C.-H.; Belopolski, I.; Alidoust, N.; Sanchez, D.S.; Zheng, H.; et al. Magnetic and Noncentrosymmetric Weyl Fermion Semimetals in the *R*AlGe Family of Compounds (*R* = Rare Earth). *Phys. Rev. B* **2018**, *97*, 041104. [CrossRef]
13. Yao, X.; Verma, R.; Graf, D.E.; Yang, H.Y.; Bahrami, F.; Zhang, R.; Aczel, A.A.; Subedi, S.; Torchinsky, D.H.; Sun, J.; et al. Topological Spiral Magnetism in the Weyl Semimetal SmAlSi. *arXiv* **2022**, arXiv:2206.05121.
14. Gaudet, J.; Yang, H.-Y.; Baidya, S.; Lu, B.; Xu, G.; Zhao, Y.; Rodriguez-Rivera, J.A.; Hoffmann, C.M.; Graf, D.E.; Torchinsky, D.H.; et al. Weyl-Mediated Helical Magnetism in NdAlSi. *Nat. Mater.* **2021**, *20*, 1650. [CrossRef]
15. Puphal, P.; Pomjakushin, V.; Kanazawa, N.; Ukleev, V.; Gawryluk, D.J.; Ma, J.; Naamneh, M.; Plumb, N.C.; Keller, L.; Cubitt, R.; et al. Topological Magnetic Phase in the Candidate Weyl Semimetal CeAlGe. *Phys. Rev. Lett.* **2020**, *124*, 017202. [CrossRef]
16. Meng, B.; Wu, H.; Qiu, Y.; Wang, C.; Liu, Y.; Xia, Z.; Yuan, S.; Chang, H.; Tian, Z. Large Anomalous Hall Effect in Ferromagnetic Weyl Semimetal Candidate PrAlGe. *APL Mater.* **2019**, *7*, 051110. [CrossRef]
17. Destraz, D.; Das, L.; Tsirkin, S.S.; Xu, Y.; Neupert, T.; Chang, J.; Schilling, A.; Grushin, A.G.; Kohlbrecher, J.; Keller, L.; et al. Magnetism and Anomalous Transport in the Weyl Semimetal PrAlGe: Possible Route to Axial Gauge Fields. *NPJ Quantum Mater.* **2020**, *5*, 5. [CrossRef]
18. Yang, H.-Y.; Singh, B.; Lu, B.; Huang, C.-Y.; Bahrami, F.; Chiu, W.-C.; Graf, D.; Huang, S.-M.; Wang, B.; Lin, H.; et al. Transition from Intrinsic to Extrinsic Anomalous Hall Effect in the Ferromagnetic Weyl Semimetal $PrAlGe_{1-x}Si_x$. *APL Mater.* **2020**, *8*, 011111. [CrossRef]

19. Wang, J.-F.; Dong, Q.X.; Huang, Y.F.; Wang, Z.S.; Guo, Z.P.; Wang, Z.J.; Ren, Z.A.; Li, G.; Sun, P.J.; Dai, X.; et al. Temperature Dependent Quantum Oscillations at a Constant Magnetic Field in a Magnetic Weyl Semimetal. *arXiv* **2022**, arXiv:2201.06412, 06412.
20. Piva, M.M.; Souza, J.C.; Brousseau-Couture, V.; Pakuszewski, K.R.; John, J.K.; Adriano, C.; Côté, M.; Pagliuso, P.G.; Nicklas, M. Tuning the Nontrivial Topological Properties of the Weyl Semimetal CeAlSi. *arXiv* **2021**, arXiv:2111.05742, 05742.
21. He, X.; Li, Y.; Zeng, H.; Zhu, Z.; Cao, C.; Luo, Y. Pressure Tuning Domain-Wall Chirality in Noncentrosymmetric Magnetic Weyl Semimetal CeAlGe. *arXiv* **2022**, arXiv:2207.08442.
22. Sanchez, D.S.; Chang, G.; Belopolski, I.; Lu, H.; Yin, J.-X.; Alidoust, N.; Xu, X.; Cochran, T.A.; Zhang, X.; Bian, Y.; et al. Observation of Weyl Fermions in a Magnetic Non-centrosymmetric Crystal. *Nat. Commun.* **2020**, *11*, 3356. [CrossRef] [PubMed]
23. Zhao, J.; Liu, W.; Rahman, A.U.; Meng, F.; Ling, L.; Xi, C.; Tong, W.; Bai, Y.; Tian, Z.; Zhong, Y.; et al. Field-Induced Tricritical Phenomenon and Magnetic Structures in Magnetic Weyl Semimetal Candidate NdAlGe. *New J. Phys.* **2022**, *24*, 013010. [CrossRef]
24. Schmehr, J.L.; Wilson, S.D. Active Crystal Growth Techniques for Quantum Materials. *Annu. Rev. Mater. Res.* **2017**, *47*, 153. [CrossRef]
25. Basov, D.N.; Averitt, R.D.; Hsieh, D. Towards Properties on Demand in Quantum Materials. *Nat. Mater.* **2017**, *16*, 1077. [CrossRef]
26. Samarth, N. Quantum Materials Discovery from a Synthesis Perspective. *Nat. Mater.* **2017**, *16*, 1068. [CrossRef]
27. Bobowski, J.S.; Kikugawa, N.; Miyoshi, T.; Suwa, H.; Xu, H.-S.; Yonezawa, S.; Sokolov, D.A.; Mackenzie, A.P.; Maeno, Y. Improved Single-Crystal Growth of Sr_2RuO_4. *Condens. Matter* **2019**, *4*, 6. [CrossRef]
28. Ito, T.; Ushiyama, T.; Yanagisawa, Y.; Tomioka, Y.; Shindo, I.; Yanase, A. Laser-Diode-Heated Floating Zone (LDFZ) Method Appropriate to Crystal Growth of Incongruently Melting Materials. *J. Cryst. Growth* **2013**, *363*, 264. [CrossRef]
29. Rey-García, F.; Ibáñez, R.; Angurel, L.A.; Costa, F.M.; de la Fuente, G.F. Laser Floating Zone Growth: Overview, Singular Materials, Broad Applications, and Future Perspectives. *Crystals* **2020**, *11*, 38. [CrossRef]
30. Kaneko, Y.; Tokura, Y. Floating Zone Furnace Equipped with a High Power Laser of 1 kW Composed of Five Smart Beams. *J. Cryst. Growth* **2020**, *533*, 125435. [CrossRef]
31. Admasu, A.S.; Vavilapalli, D.S. The Laser-Diode Heated Floating Zone Method for Automated Optimal Synthesis of Refractory Oxides and Alloys. *arXiv* **2021**, arXiv:2103.05587.
32. Neubauer, A.; Jonietz, F.; Meven, M.; Georgii, R.; Brandl, G.; Behr, G.; Böni, P.; Pfleiderer, C. Optical Floating Zone Growth of High-Quality Cu_2MnAl Single Crystals. *Nucl. Instrum. Methods Phys. Res. A* **2012**, *688*, 66. [CrossRef]
33. Brunt, D.; Hatnean, M.C.; Petrenko, O.A.; Lees, M.R.; Balakrishnan, G. Single-Crystal Growth of Metallic Rare-Earth Tetraborides by the Floating-Zone Technique. *Crystals* **2019**, *9*, 211. [CrossRef]
34. Amigó, M.L.; Maljuk, A.; Manna, K.; Stahl, Q.; Felser, C.; Hess, C.; Wolter, A.U.B.; Geck, J.; Seiro, S.; Büchner, B. Laser-Assisted Floating Zone Growth of $BaFe_2S_3$ Large-Sized Ferromagnetic-Impurity-Free Single Crystals. *Crystals* **2021**, *11*, 758. [CrossRef]
35. Sinha, M.; Vivanco, H.K.; Wan, C.; Siegler, M.A.; Stewart, V.J.; Pogue, E.A.; Pressley, L.A.; Berry, T.; Wang, Z.; Johnson, I.; et al. Twisting of 2D Kagomé Sheets in Layered Intermetallics. *ACS Cent. Sci.* **2021**, *7*, 1381. [CrossRef] [PubMed]
36. Bauer, A.; Neubauer, A.; Münzer, W.; Regnat, A.; Benka, G.; Meven, M.; Pedersen, B.; Pfleiderer, C. Ultra-High Vacuum Compatible Induction-Heated Rod Casting Furnace. *Rev. Sci. Instrum.* **2016**, *87*, 063909. [CrossRef]
37. Nagai, I.; Shirakawa, N.; Ikeda, S.-I.; Iwasaki, R.; Nishimura, H.; Kosaka, M. Highest Conductivity Oxide $SrMoO_3$ Grown by a Floating-Zone Method under Ultralow Oxygen Partial Pressure. *Appl. Phys. Lett.* **2005**, *87*, 024105. [CrossRef]
38. Mao, Z.Q.; Maeno, Y.; Fukazawa, H. Crystal Growth of Sr_2RuO_4. *Mater. Res. Bull.* **2000**, *35*, 1813. [CrossRef]
39. Perry, R.S.; Maeno, Y. Systematic Approach to the Growth of High-Quality Single Crystals of $Sr_3Ru_2O_7$. *J. Cryst. Growth* **2004**, *271*, 134. [CrossRef]
40. Zhou, M.; Hooper, J.; Fobes, D.; Mao, Z.Q.; Golub, V.; O'Connor, C.J. Electronic and Magnetic Properties of Triple-Layered Ruthenate $Sr_4Ru_3O_{10}$ Single Crystals Grown by a Floating-Zone Method. *Mater. Res. Bull.* **2005**, *40*, 942. [CrossRef]
41. Kikugawa, N.; Balicas, L.; Mackenzie, A.P. Physical Properties of Single-Crystalline $CaRuO_3$ Grown by a Floating-Zone Method. *J. Phys. Soc. Jpn.* **2009**, *78*, 014701. [CrossRef]
42. Kikugawa, N.; Baumbach, R.; Brooks, J.S.; Terashima, T.; Uji, S.; Maeno, Y. Single-Crystal Growth of a Perovskite Ruthenate $SrRuO_3$ by the Floating-Zone Method. *Cryst. Growth Des.* **2015**, *15*, 5573. [CrossRef]
43. Kikugawa, N.; Sokolov, D.A.; Nagasawa, T.; Mackenzie, A.P. Single-Crystal Growth of Sr_2RuO_4 by the Floating-Zone Method Using an Infrared Image Furnace with Improved Halogen Lamps. *Crystals* **2021**, *11*, 392. [CrossRef]
44. Martien, D.; Williamsen, M.; Spagna, S.; Black, R.; DaPron, T.; Hogan, T.; Snow, D. An Ultrasensitive Differential Capacitive Dilatometer. *IEEE Trans. Magn.* **2019**, *55*, 1. [CrossRef]
45. Gschneidner, K.A.; Pecharsky, V.K. Magnetocaloric Materials. *Annu. Rev. Mater. Sci.* **2000**, *30*, 387. [CrossRef]
46. Wang, T.; Guo, Y.; Wang, C.; Yang, S. Correlation between Non-centrosymmetic Structure and Magnetic Properties in Weyl Semimetal NdAlGe. *Solid State Commun.* **2020**, *321*, 114041. [CrossRef]
47. Barron, T.H.K.; White, G.K. *Heat Capacity and Thermal Expansion at Low Temperatures*; Kluwer Academic/Plenum: New York, NY, USA, 1999.
48. Tishin, A.M. *Magnetocaloric Effect: From Theory to Practice, in Encyclopedia of Materials: Science and Technology*; Buschow, K.H.J., Cahn, R.W., Flemings, M.C., Ilschner, B., Kramer, E.J., Mahajan, S., Veyssière, P., Eds.; Elsevier: Oxford, UK, 2001; pp. 5035–5041.
49. Patra, M.; Majumdar, S.; Giri, S.; Xiao, Y.; Chatterji, T. Magnetic, Magnetocaloric and Magnetoresistive Properties of Cubic Laves Phase $HoAl_2$ Single Crystal. *J. Phys. Condens. Matter* **2014**, *26*, 046004. [CrossRef]
50. Pecharsky, V.K.; Gschneidner, K.A., Jr. Giant Magnetocaloric Effect in $Gd_5(Si_2Ge_2)$. *Phys. Rev. Lett.* **1997**, *78*, 4494. [CrossRef]

51. Fujieda, S.; Fujita, A.; Fukamichi, K. Large Magnetocaloric Effect in La(Fe_xSi_{1-x})$_{13}$ Itinerant-Electron Metamagnetic Compounds. *Appl. Phys. Lett.* **2002**, *81*, 1276. [CrossRef]
52. Gupta, S.; Suresh, K.G. Review on Magnetic and Related Properties of *RTX* Compounds. *J. Alloys Compd.* **2015**, *618*, 562. [CrossRef]
53. Krenke, T.; Duman, E.; Acet, M.; Wassermann, E.F.; Moya, X.; Mañosa, L.; Planes, A. Inverse Magnetocaloric Effect in Ferromagnetic Ni-Mn-Sn Alloys. *Nat. Mater.* **2005**, *4*, 450. [CrossRef] [PubMed]
54. Van Peski-Tinbergen, T.; Dekker, A.J. Spin-Dependent Scattering and Resistivity of Magnetic Metals and Alloys. *Physica* **1963**, *29*, 917. [CrossRef]
55. Maki, S.; Adachi, K. Antiferromagnetism and Weak Ferromagnetism of Disordered Bcc Cr-Mn Alloys. *J. Phys. Soc. Jpn.* **1979**, *46*, 1131. [CrossRef]
56. Terashima, T.; Kikugawa, N.; Kasahara, S.; Watashige, T.; Shibauchi, T.; Matsuda, Y.; Wolf, T.; Böhmer, A.E.; Hardy, F.; Meingast, C.; et al. Pressure-Induced Antiferromagnetic Transition and Phase Diagram in FeSe. *J. Phys. Soc. Jpn.* **2015**, *84*, 063701. [CrossRef]